SOFT ROBOTICS
Volume 8, Number 1, 2021

DOI: 10.1089/soro.2019.0011

SoRo
Soft Robotics

ORIGINAL ARTICLE

Soft Miniaturized Actuation and Sensing Units for Dynamic Force Control of Cardiac Ablation Catheters

Nitish Kumar,[1] Jackson Wirekoh,[2] Samir Saba,[3] Cameron N. Riviere,[4] and Yong-Lae Park[4,5]

Abstract

Recently, there has been active research in finding robotized solutions for the treatment of atrial fibrillation (AF) by augmenting catheter systems through the integration of force sensors at the tip. However, limited research has been aimed at providing automatic force control by also integrating actuation of the catheter tip, which can significantly enhance safety in such procedures. This article solves the demanding challenge of miniaturizing both actuation and sensing for integration into flexible catheters. Fabrication strategies are presented for a series of novel soft thick-walled cylindrical actuators, with embedded sensing using eutectic gallium–indium. The functional catheter tips have a diameter in the range of 2.6–3.6 mm and can both generate and detect forces in the range of < 0.4 N, with a bandwidth of 1–2 Hz. The deformation modeling of thick-walled cylinders with fiber reinforcement is presented in the article. An experimental setup developed for static and dynamic characterization of these units is presented. The prototyped units were validated with respect to the design specifications. The preliminary force control results indicate that these units can be used in tracking and control of contact force, which has the potential to make AF procedures much safer and more accurate.

Keywords: medical robotics, soft actuators, soft sensors, force control, cardiac ablation, catheters

Introduction

Soft robotics technology is finding increased visibility in biomedical applications[1] due to the inherent compliance and safety of soft medical devices during intimate interaction with human tissues. Although soft robotics technology has become increasingly prominent in the design of rehabilitative and prosthetic devices,[2–5] difficulty in miniaturization of soft actuation and sensing has been a limiting factor in the design of integrated compact systems for applications in minimally invasive surgery (MIS).[6–8]

MIS treatments[9] are characterized by keyhole surgeries in which a system equipped with a functional tip is inserted through a small port in the body. Due to the nature of MIS operations, patients experience shorter recovery times and higher success rates.[10,11] Most MIS procedures are performed for diagnostic purposes, through localized biopsies,[12,13] or for the localized destruction of abnormal cells, such as in the case of cardiac ablation.

Cardiac ablation,[14] which involves localized destruction of abnormal heart tissues, is one of the most-performed MIS procedures with 30,000–35,000 being conducted annually for the treatment of atrial fibrillation (AF). Radio frequency ablation (RFA) is one of the main techniques used in cardiac ablation procedures. The traditional medical device for RFA consists of a flexible sheath into which a catheter equipped with a functional tip is inserted. This functional tip, when in contact with a heart, destroys the abnormal cells by transferring energy through a system of electrodes.

The typical surgical workflow for cardiac ablation begins with the insertion of the sheath through a vein in the groin. The sheath is then moved to the heart. The catheter equipped with its functional tip is then inserted into the sheath, which serves as a guide. The physician steers the catheter along the sheath until it makes contact with the abnormal heart tissue. Subsequently, the physician manually manipulates the position of the catheter tip by applying force at the proximal

[1]Department of Computer Science, ETH Zürich, Zürich, Switzerland.
[2]NYU Langone Health, New York City, New York, USA.
[3]Department of Cardiac Electrophysiology, University of Pittsburgh Medical Center, Pittsburgh, Pennsylvania, USA.
[4]Robotics Institute, Carnegie Mellon University, Pittsburgh, Pennsylvania, USA.
[5]Department of Mechanical Engineering, Institute of Advanced Machines and Design, Institute of Engineering Research, Seoul National University, Seoul, Korea.

end of the catheter, indirectly controlling the contact force between the tip and the target tissue.

The required amount of energy and the lesion size, in the case of RFA, are determined by the interaction of the contact force between the tip and the tissue.[15] Unfortunately, manual control of the catheter tip results in large variations in applied force.[16,17] In some cases, complications, such as perforation, arise due to the application of excessive force.[18] In contrast, if the force is too small, the duration of ablation is prolonged, and the lesion size consequently becomes larger than necessary.

Researchers have attempted to alleviate this issue through the integration of force sensors in preexisting catheter tips.[19,20] These sensors could be used to provide visual/haptic feedback or coupled with external/*in situ* actuation for active control of contact forces. However, a discussion on integration of these sensors with suitable actuation technologies and contact force control is missing. The integration and active control of contact forces has the potential to eliminate complications which may arise due to variations in the manual response and reaction times between physicians.

In recent studies, alternative solutions have been sought by developing systems to provide automatic force control of the catheter tip by externally controlling the catheter handle.[21,22] With this strategy, however, the modeling of the system becomes increasingly complex due to the presence of friction caused by random contacts between the sheath and the catheter, as well as viscous forces caused by the motion between the catheter and the sheath *in vivo*. In addition, the physician does not retain control over the catheter inside the sheath and the overall procedure in this workflow.

There has been an approach to address these problems through the design of a miniaturized end-effector integrating an off-the-shelf piezoelectric actuator ($2.8 \times 2.8\,mm^2$ cross-sectional area, 6 mm length) combined with fiber optic (fiber Bragg gratings) force sensing.[23]

However, the main drawback in this design was the choice of rigid components for both actuation (rigid actuator) and sensing (optical fibers + deformable element). Commercially available catheter sheaths, designed to provide navigation for the catheters to the site of treatment, restrict the external diameter of ablation catheters to 2–5 mm. Moreover, the catheter tip needs to bend and traverse the flexible sheath, which takes the shapes of the veins into which it is inserted. The use of rigid components in this catheter tip system, both for actuation and sensing, resulted in an inflexible 26 mm section, which limits possible bending angles, making navigation of the catheter more difficult in the flexible sheath. In addition, the actuator choice limits the force output and displacement to 0.5 N and 5 mm, respectively, with currently no flexibility to modify the design for other similar applications with different requirements.

To overcome these limitations, a miniaturized flexible tip containing integrated actuation and sensing, which could be embedded at the tip of conventional catheters, has been designed and prototyped in the current work, as shown in Figure 1. The miniaturized catheter tip is composed of a soft fiber-reinforced hydraulic thick-walled cylindrical actuator and a soft force sensor, fabricated from eutectic gallium–indium (eGaIn).[24–26] The liquid metal eGaIn was used for preliminary design feasibility due to its flexibility in electronic hardware prototyping, simple circuitry for signal processing and data collection, and low toxicity levels.[27–30] However, future designs will focus on identifying the optimal nontoxic liquid metal or ionic liquid to be used for *in vivo* sensing.

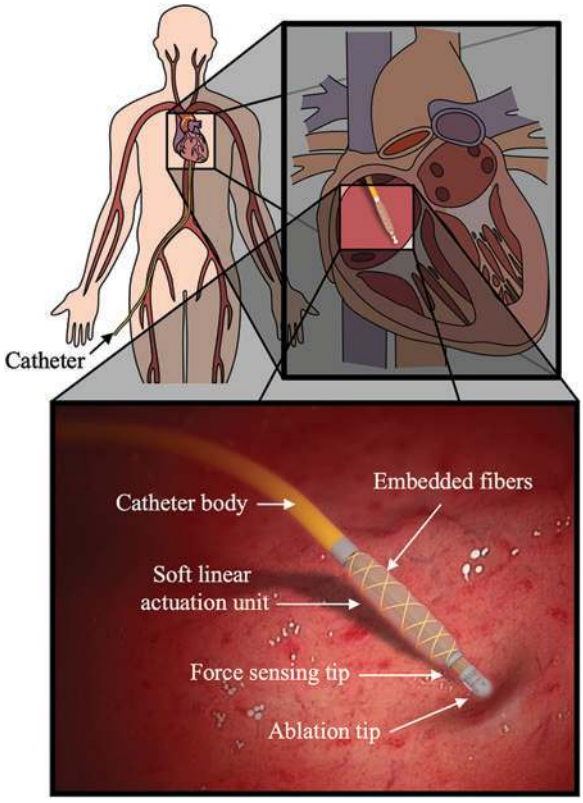

FIG. 1. Conceptual design of cardiac ablation catheter integrated with soft actuation and sensing unit for dynamic force control. Color images are available online.

The main contribution of this work is in the design, modeling, and experimental evaluation of a miniaturized soft sensing and actuation unit, which meets the requirements of cardiac ablation procedures. The advantage of our approach lies in the development of the capability to do *in situ* actuation of the catheter tip, as opposed to external actuation, through the integration of a soft miniaturized actuation and sensing unit for MIS procedures. With *in situ* actuation and sensing, the system modeling and force control become less complex due to absence of transmission mechanism with variable contacts along the veins and capillaries. Furthermore, this design keeps the manual control of the catheter in the hands of the physician, which is desirable for safety.

Fabrication of the soft thick-walled cylindrical actuators with embedded soft sensing elements was described. In addition, an exact analytical hyperelastic model for a soft fiber-reinforced thick-walled cylindrical actuator was detailed. An experimental setup was developed to use hydraulic actuation rather than pneumatics, which are typical in pneumatic artificial muscles (PAMs),[31,32] so as to be inherently safer in case of accidental leaks. Medical grade saline solution was used as a medium for hydraulic actuation. Through this experimental apparatus, the static and dynamic characterization of both the soft sensing and actuation elements shows that they adhere to the required specifications.

The rest of the article is organized as follows. The required specifications are first listed for the development and

experimental validation of the designed miniaturized actuation and sensing unit. This is followed by the hyperelastic modeling of the designed unit, providing theoretical parameterization and characterization of the unit. The fabrication and prototyping strategy of a series of such units with different parameters is then described. The experimental setup and the results with the static and dynamic characterization of the developed unit, including preliminary force control, are presented in the following section. The article finally provides conclusions and perspectives for the current and future work.

Design Specifications

This section details the specifications for the mechanical design, including static and dynamic performance of the developed miniaturized sensing and actuation unit. These parameters were derived from the necessary specifications required for cardiac ablation procedures intended for treatment of AF.

Size

A catheter sheath is first inserted into the blood vessel through which a catheter is later inserted for the AF treatment. The diameter of the catheter sheath and the catheter is dependent on the size of the blood vessels, which usually ranges between 6F and 15F (2–5 mm).

Actuation

Apart from the constraints on the size, the miniaturized actuation must be able to apply a force in the range of 0–0.4 N,[17] which is observed during diverse catheter ablation procedures for the AF treatment. Since the catheter tip should remain in contact with the heart wall during the procedure, limits on the linear displacement and the linear speed of the actuator should be enough to compensate for the heart wall movement (1–2 mm at 1–2 Hz) caused by the beating of the heart and expansion/contractions of the lungs during breathing (7–8 mm).[33] In addition, actuators should maintain a safe operating pressure range commiserate with pressurized systems used in the heart and veins such as stents, which places a limit of pressures to a safe range of 0–1.5 MPa.[34]

Force sensing

Catheter ablation, while taking place in a three-dimensional (3D) space, is considered as a uniaxial treatment. Currently, the catheter sheath is used to direct the catheter to the site of treatment, bending and twisting to fit the contours of the veins and capillaries. Physicians then apply axial forces to the catheter allowing it to displace axially along the alignment of the catheter sheath's end effector. Due to this, at least one degree of freedom (DOF) in the force sensing is required to measure the interaction force between the tip and the heart tissue. The force sensor should be able to measure force within the range 0–0.4 N with a resolution of 0.01 N, which is the same as required for the actuation. Moreover, it should have a bandwidth within 1–2 Hz.

Modeling

Soft actuators, most notably PAMs or McKibben muscles in prior research,[35–37] have been developed without the aspect of miniaturization in mind. The external diameter and applicable forces in prior research are several times larger than would be needed for a MIS procedure, especially if the soft actuator forms the local interface between the surgical tool and the tissue in contact. Consequently, the use of soft actuators in MIS procedures has been largely limited to PAMs, which are placed remotely in the surgical tool away from any contact with the human tissue.[38]

Due to small radial thicknesses in comparison to external radii, PAMs found in prior work are often classified as thin-walled cylindrical shells under the common modeling assumption of vanishing stress through the thickness; see modeling of thin-walled cylindrical shells[39,40] and fiber-reinforced actuators.[41,42] However, miniaturization leads to the consideration of PAM designs, which do not satisfy this assumption. In this case, thin-walled approximations predict required input pressures that are one to two orders of magnitude higher than what is actually required to achieve expected force and displacement ranges. This section builds upon theory for elastic thick-walled cylindrical shells,[43,44] to provide an exact solution for hyperelastic fiber-reinforced thick-walled cylindrical actuators using the general approach of strain-energy minimization.

The design concept, as shown in Figure 2a, consists of a thick-walled cylindrical shell, with fiber reinforcement. One closed end acts as the soft deformable element fabricated out of a hyperelastic material. Upon application of fluid pressure inside, the element deforms and expands both radially and axially. The controlled axial deformation is of most interest in this article. Moreover, a microchannel with a U shape was embedded in the closed end of the cylinder, which was filled with a conductive liquid (eGaIn).

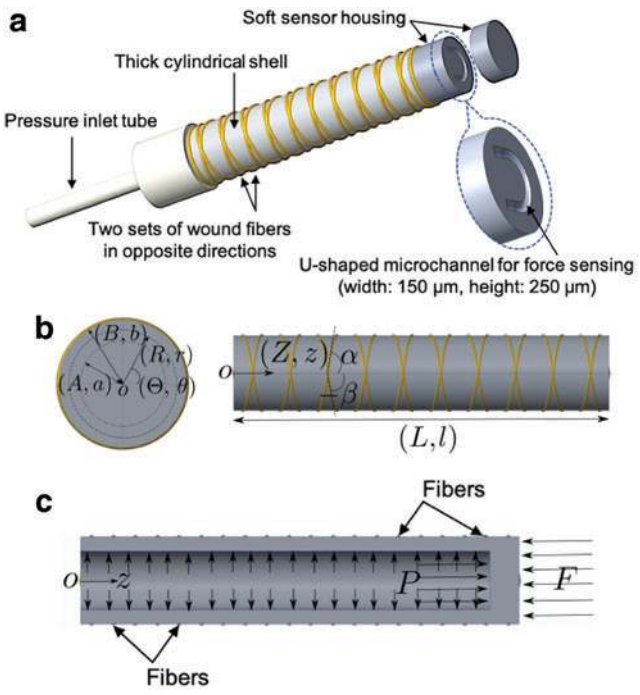

FIG. 2. **(a)** Design of miniaturized soft actuation and sensing unit. **(b)** Selected cylindrical coordinates and parameterization: front (*left*) and side (*right*) views. **(c)** Sectioned view of the actuator: equilibrium under action of external force F and internal pressure P. Color images are available online.

In this section, we will develop the exact analytical model for thick-walled cylindrical actuators with fiber reinforcement. For the thin-walled assumption to hold, the ratio of radius to wall thickness must be >10. The size requirements for application along with practical design and prototyping considerations, which will be described in detail in the following sections, put the soft actuators considered in the article under the category of thick-walled cylindrical shells. The radius to the wall thickness for the actuators is <3.6 (1.8/0.5 mm).

Figure 2b shows the parameterization of these thick-walled cylindrical actuators with fiber reinforcement. Given the geometry of the actuators, a cylindrical coordinate system is used. We adopted the parameterization as utilized in Haughton and Ogden[43] so as to compare the results easily. Nonetheless, for completeness a brief description is given here, and the full details can be found in Haughton and Ogden.[43]

The variables R, Θ, and Z are cylindrical coordinates for the undeformed configuration represented by Equation (1), whereas the variables r, θ, and z are cylindrical coordinates for the deformed configuration represented by Equation (2). The variables A and a are internal radii before and after deformation, respectively. The variables B and b are external radii before and after deformation, respectively. The variables α and $-\beta$ are the helix angles for the two sets of fibers. The variables L and l are lengths before and after deformation, respectively.

$$A \le R \le B, \;\; 0 \le \Theta \le 2\pi, \;\; 0 \le Z \le L \tag{1}$$

$$a \le r \le b, \; 0 \le \theta \le 2\pi, \; 0 \le z \le l \tag{2}$$

Let λ_1, λ_2, and λ_3 be the principal stretches as defined in Equation (3). The material is assumed to be incompressible such that the relationship $\lambda_1\lambda_2\lambda_3 = 1$ holds. Let $W \equiv W(\lambda_1\lambda_2\lambda_3)$ be the strain energy density function per unit volume, which can be expressed after eliminating λ_3 as $W \equiv W\left(\lambda_1, \; \lambda_2, \; \lambda_1^{-1}\lambda_2^{-1}\right)$. Let us also define $\lambda_a = \frac{a}{A}$ and $\lambda_b = \frac{b}{B}$, and let P be the internal inflation pressure.

$$\lambda_1 = \frac{r}{R} = \lambda, \;\; \lambda_2 = \lambda_z = \lambda_l = \frac{l}{L}, \;\; \lambda_3 = (\lambda_1\lambda_2)^{-1} \tag{3}$$

The incompressibility condition can also be rewritten as a condition for constant volume of the cylindrical shell.

$$\pi\left(r^2 - a^2\right)l = \pi\left(R^2 - A^2\right)L \tag{4}$$

$$\lambda_a^2\lambda_l - 1 = \frac{R^2}{A^2}\left(\lambda^2\lambda_l - 1\right) = \frac{B^2}{A^2}\left(\lambda_b^2\lambda_l - 1\right) \tag{5}$$

In Haughton and Ogden,[43] the equilibrium condition for thick-walled cylindrical shells is used for derivation for expression of internal inflation pressure P. However, as will be shown later, these expressions are valid only for thick-walled cylindrical actuators without fiber reinforcement.

For modeling of fiber-reinforced thick-walled cylindrical actuators, instead of starting from the expression for differential equilibrium, we will use the general approach of minimization of the total energy under geometric constraints of inextensibility of fibers and incompressibility of the hyperelastic material. The actuator is subject to internal inflation pressure P and an external force F acting along the axis of the cylinder at the closed end, as shown in Figure 2c.

This external force F is the contact force between the actuator and the heart tissue during cardiac ablation procedures, which needs to be controlled. Let E be the total energy, $E1$ be the total strain energy, $E2$ be the total work done under pressure P, and $E3$ be the total work done under external force F. The corresponding expressions are derived and presented in Equations (6–8).

$$E1 = 2\pi l \int_a^b \hat{W}\, r dr = 2V_0\lambda_l\left(1 - \lambda_a^2\lambda_l\right)\int_{\lambda_a}^{\lambda_b} \frac{\hat{W}\,\lambda d\lambda}{\left(1 - \lambda^2\lambda_l\right)^2} \tag{6}$$

$$E2 = -V_0P\left(\lambda_a^2\lambda_l - 1\right), \;\; E3 = FL(\lambda_l - 1) \tag{7}$$

$$E(\lambda_a, \; \lambda_b, \; \lambda_l) = E1 + E2 + E3, \;\; V_0 = \pi A^2 L \tag{8}$$

This shows that the total energy is a function of three stretches, λ_a, λ_b, and λ_l. Equation (5) gives a relationship between λ_a and λ_b such that $\lambda_b = \Lambda_b(\lambda_a)$. Thus,

$$\hat{E}(\lambda_a, \lambda_l) = 2V_0\lambda_l\left(1 - \lambda_a^2\lambda_l\right)\int_{\lambda_a}^{\Lambda_b} \frac{\hat{W}\,\lambda d\lambda}{\left(1 - \lambda^2\lambda_l\right)^2} - V_0P\left(\lambda_a^2\lambda_l - 1\right) + FL(\lambda_l - 1) \tag{9}$$

Without fiber reinforcement, λ_a and λ_l are independent. Differentiating $E(\lambda_a, \lambda_l)$ with respect to λ_a and setting $\frac{\partial E}{\partial \lambda_a} = 0$ then gives exactly the expression for P as derived in Polygerinos *et al.*[41] Therefore, the expression for P, as derived in Polygerinos *et al.*,[41] does not hold when fiber reinforcement is considered and λ_a, λ_l are no longer independent.

To complete the modeling for thick-walled fiber-reinforced cylindrical actuators, we added the geometric constraint arising from inextensibility of the fiber. Let k be the length of the fiber. The Equation (10) represents the inextensibility constraint formulated for thick-walled cylindrical actuators with fibers wound externally and gives a relationship between λ_b and λ_l. For a nonbending motion, angle α must be equal to angle $-\beta$.[40]

$$\alpha = -\beta, \;\; k\cos\alpha = \lambda_l L, \;\; \lambda_b^2\left(k^2 - L^2\right) = k^2 - \lambda_l^2 L^2 \tag{10}$$

Thus, the expression for the total energy $\hat{E}$ is a function of only λ_l and is obtained in Equation (11). Differentiating E with respect to λ_l and setting $\frac{dE}{d\lambda_l} = 0$ gives the desired relationship between the inlet pressure P, the external contact force F, and the axial stretch λ_l as a function of the design (L, A, B, α) and material (E_a is 100% tensile modulus reported in the material data sheet) parameters for the thick-walled fiber-reinforced cylindrical actuators. The radial stretches λ_a and λ_b can be obtained from Equations (5) and (10) in terms of λ_l such that $\lambda_a = \Lambda_a(\lambda_l)$ and $\lambda_b = \Lambda_b(\Lambda_a(\lambda_l))$.

$$\hat{E}(\lambda_l) = 2V_0\lambda_l\left(1 - \Lambda_a^2\lambda_l\right)\int_{\Lambda_a}^{\Lambda_b} \frac{\hat{W}\,\lambda d\lambda}{\left(1 - \lambda^2\lambda_l\right)^2} - V_0P\left(\Lambda_a^2\lambda_l - 1\right) + FL(\lambda_l - 1) \tag{11}$$

Design

A functional catheter tip was designed and fabricated to satisfy the system requirements, as laid out in Section-Design Specifications, for the treatment of AF through a catheter ablation procedure. Specifically, the prototype device incorporates two major systems, a soft hydraulic actuator and a soft force sensor. To ensure a compact, compliant, and effective design, soft materials were utilized to produce the embedded actuation and sensing components of the functional catheter tip.

The soft actuator is composed of a deformable thick-walled cylindrical shell, fabricated by curing a silicone elastomer (Dragon Skin 30 or Smooth-Sil 935; Smooth-On, Inc.) in a 3D printed mold. The cured elastomer is then geometrically constrained by a double helix of inextensible fibers (Kevlar 69 Thread; McMaster Carr). The two sets of fibers are wrapped at helix angles, $\alpha = 75°$ and $-\beta = 75°$. During pressurization with saline solution, chosen for safety reasons, the soft actuator deforms radially and axially. In this study, the constraint induced by the fiber reinforcements plays a particularly important role, minimizing unwanted deformation in the radial direction. This decreases the occurrence of bending due to imperfections in fabrication, while producing repeatable linear displacements in the axial direction of the actuator.

The soft force sensor is composed of a solid cylindrical section, made from a softer material (Dragon Skin 10; Smooth-On, Inc.), which contains an embedded U-shaped microchannel filled with a liquid conductor (eGaIn; Alfa Aesar) for resistive sensing. The microchannel has a width of 0.15 mm and a height of 0.25 mm. Forces applied to this section cause the microchannel to deform, which in turn causes an increase in the sensor's electrical resistance.

The actuation section has the length of $L = 15$ mm and an internal radius of $A = 0.8$ mm for all the prototypes. Prototypes with two external radii of $B = 1.3$ and 1.8 were produced. The sensor section has a length of 2.75 mm and an external diameter of 2.6 and 3.8 mm, respectively, for actuator prototypes with external radii of $B = 1.3$ and 1.8.

Fabrication

The soft catheter tip was fabricated in a multistep process, as shown in Figure 3a, using customized 3D printed molds (Objet 30; Stratasys) and room temperature-vulcanizing silicone elastomer.

First, the actuation section was fabricated using silicone elastomer. Four different catheter tip prototypes were fabricated in this work, as shown in Figure 3b. The first two (1 and 2) were made of Dragon Skin 30 ($E_a = 0.614$ MPa), and the other two (3 and 4) were made of Smooth-Sil 935 ($E_a = 1.173$ MPa). A stainless steel rod, 1.6 mm in diameter, was aligned in the mold, which contained extrusions to demarcate where the fibers should be wound.

Next, the silicone elastomer was poured into the mold and sealed with an end cap containing an extruded cylinder, to cordon off a section for the sensor. The material was then allowed to cure. After curing, the end-cap was removed. Subsequently, Dragon Skin 10 ($E_a = 0.151$ MPa), a softer silicone elastomer, was mixed and poured into the mold to fill the previously blocked section.

Next, a second end-cap, containing the negative of the microchannel layout, was placed. Following this second curing process, the microchannel was sealed and filled with eGaIn.

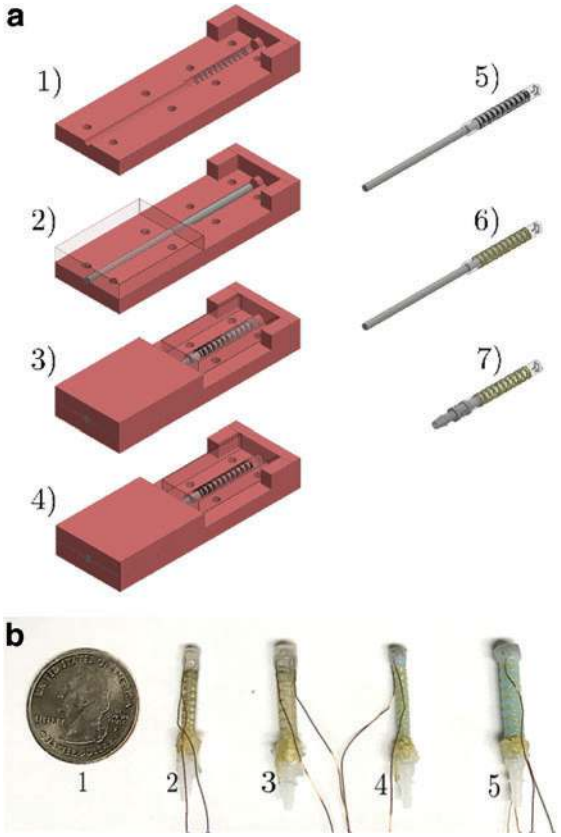

FIG. 3. **(a)** Fabrication process of fiber-reinforced functional catheter tip: 1) prepare *bottom* core mold and front cap section with extruded cylinder, 2) place steel rod used to make inner diameter of catheter, 3) fill mold with uncured material, then place on *top* mold section, 4) replace front cap with cap containing negative of microchannel, 5) remove cured core from mold and fill microchannel with eGaIn, 6) wind Kevlar thread in double helix around core, 7) replace rod with inlet connector to seal section and add wires to the sensor. **(b)** From *left* to *right*: 1) U.S. quarter dollar coin, 2) prototype with Dragon Skin 30, $E_a = 0.614$ MPa, with external radius of $B = 1.3$ mm, 3) prototype with Dragon Skin 30, $E_a = 0.614$ MPa, with external radius of $B = 1.8$ mm, 4) prototype with Smooth-Sil 935, $E_a = 1.173$ MPa, with external radius of $B = 1.3$ mm, 5) prototype with Smooth-Sil 935, $E_a = 1.173$ MPa, with external radius of $B = 1.8$ mm. (E_a is 100% tensile modulus reported in material data sheet.) eGaIn, eutectic gallium–indium. Color images are available online.

Next, fibers were wound around the completed actuator section and tied in place. The 38-gauge copper magnet wire was then inserted into the reservoir section of the microchannel.

Finally, tubing and the connectors were placed and bonded to the soft actuator using Dragon Skin 10 to complete the functional catheter tip. Four representative prototypes of the actuation section were fabricated with different sizes and materials, as shown in Figure 3b. Although the theoretical model could assess the performance of the actuators, it could not predict potential issues with fabrication. Different prototype designs were used to assess the feasibility of fabricating the miniaturized actuators.

Experimental Assessment

To validate the actuation and force sensing requirements laid out in Section-Design Specifications, an active setup was needed to actuate the passive deformable element. This section describes design and development of the experimental setup, which is then used for static and dynamic characterization of the miniaturized actuation and sensing unit.

Experimental setup

Hydraulic actuation. Figure 4a describes the active setup with actuation and sensing components. A glass syringe with internal diameter of 3.26 mm (6500T55; McMaster) acts as a hydraulic cylinder, where the piston is attached to an electric linear motor (LP25–35; Nanotec) capable of applying force up to 5 N.

The piston was connected to the linear actuator with a single-axis load cell (FSAGPDXX001RCAB5; Honeywell) in between to measure the interaction force between them.

A commercial pressure sensor (HSCDRRT100PGAA5; Honeywell), which can sense pressure from 0 to 0.690 MPa, was connected to the hydraulic circuit to measure the generated internal pressure due to actuation of the syringe.

The shutoff two-way valve serves the purpose of connecting and disconnecting the hydraulic circuit to another syringe, which is used to fill the hydraulic circuit with the saline solution. Before filling the hydraulic circuit, the piston was removed completely from the syringe and then later reinserted after the hydraulic circuit had been filled. All the fixtures in the setup were fabricated using a 3D printer and a two-dimensional laser cutting machine.

Characterization setup. Figure 4b shows the extra commercial sensors used for the characterization of the soft actuator and the sensor. A laser position sensor with a resolution of 0.005 mm (OADM 12I6430/S35A; Baumer) was used for measuring the displacement of the soft actuator under pressure input measured by the pressure sensor. There was no external force applied for the soft actuator characterization. A force sensor with a resolution of 0.01 N (FSG005WNPB; Honeywell) was used for soft sensor characterization, where the tip of the soft sensor is held fixed.

Data acquisition and controls. Since the soft sensor and the commercial force sensor (FSG005WNPB; Honeywell) have unamplified outputs, two amplification boards (EMBSGB200; Tacuna Systems) were used to get the corresponding sensor output voltages. The data from the force and the displacement sensors in the setup were sampled at 100 Hz and acquired by a microcontroller (Due; Arduino). Another microcontroller (Mega 2560; Arduino) was used solely for controlling the linear actuator for generating desired pressure input profiles used for the various tests described later in the article.

Static characterization

Soft actuator. For static characterization of the soft actuators, the setup in Figure 4b-left was utilized. The linear actuator was run at a constant speed for a certain number of steps, producing ramp profiles for input pressure and corresponding output displacement of the soft actuator, as shown in Figure 5. This is a representative time-dependent input-output profile. The final input pressure may vary for different actuators. However, for the same actuator prototype, the final input pressure and ramp profile were kept the same for different trials.

The four different actuator prototypes varying in material and size, as shown in Figure 3b, were tested, and 10 datasets were collected for each actuator prototype. Figure 6 shows the static calibration curves for different actuator prototypes.

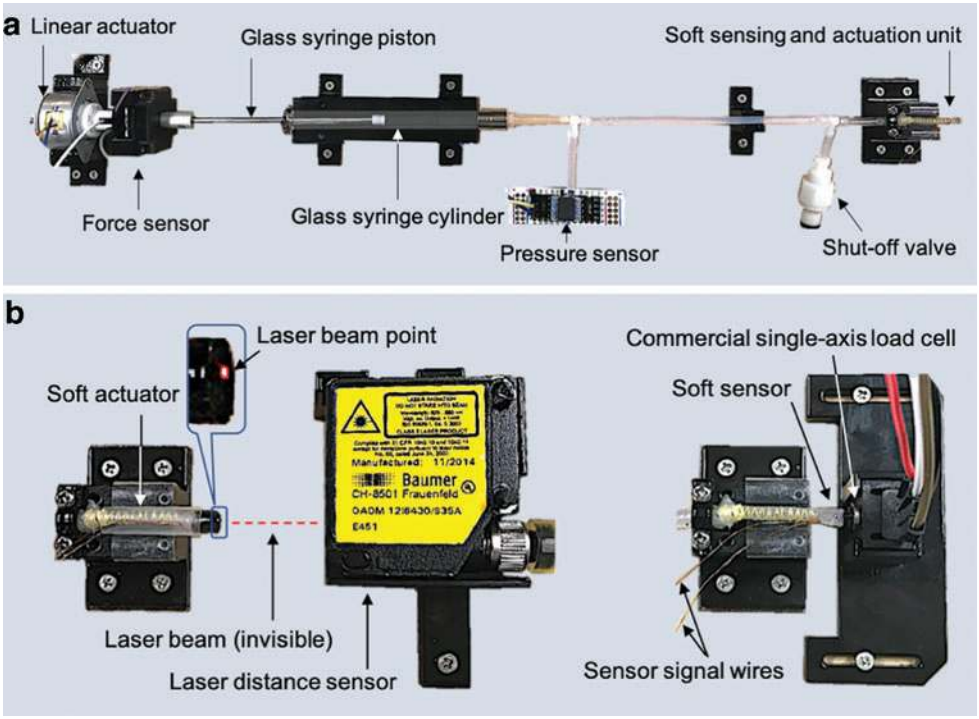

FIG. 4. **(a)** Experimental setup with active actuation and sensing components. **(b)** Characterization setup for miniaturized actuation (*left*) and sensing (*right*) unit with commercial displacement and force sensors, respectively. Color images are available online.

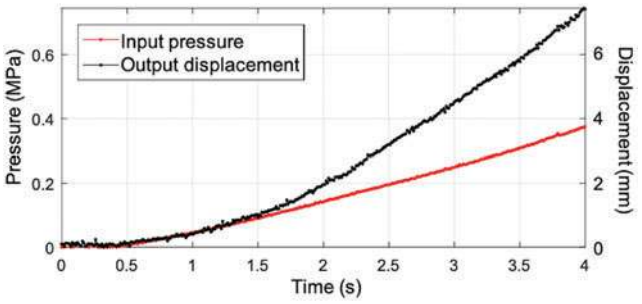

FIG. 5. Input (pressure vs. time) and output (displacement vs. time) for static characterization of soft actuator. Color images are available online.

Since the heart wall moves up to 5–8 mm over the course of catheter treatment due to the natural heartbeat, as well as breathing, the maximum displacement of the actuators was set to be at least within this range to be effective during treatment.

The black data points show the average experimental displacement captured over 10 trials. A quadratic curve was fitted to the average of the experimental data for each actuator and is plotted in red in Figure 6. The root-mean-square errors (RMSEs) for different results in Figure 6a–d are 0.141, 0.093, 0.061, and 0.157 mm, respectively. The coefficients of determination (R-squared) for different results in Figure 6a–d were 0.996, 0.996, 0.998, and 0.991, respectively.

The curve in cyan color shows the theoretical displacement when the Neo-Hookean model is chosen as the hyperelastic model and is used for computation according to the modeling of the soft thick-walled fiber-reinforced cylindrical actuators developed earlier in the Section-Modeling. The theoretical model fitted well with the experimental data for Figure 6c and d for standard reported values of E_a in the material data sheet. In Figure 6a and b, an experimentally calculated value of modulus E_a^{expr} was used to match the experimental data with the simulated data from the theoretical model.

As shown in Figure 6a, an output displacement within the range $7-8$ mm was achieved. For other actuator prototypes, as in Figure 6b–d, the output displacement of the actuator was kept around 5 mm. However, the same displacement range of $7-8$ mm can be achieved for these actuators as well at higher applied input pressure levels.

Hysteresis errors for the soft actuators, ($E_a = 0.614$ MPa) and ($E_a = 1.173$ MPa), were 14.9% and 9.6%, respectively. The hysteresis levels varied between material types, but not radii. The materials have different viscoelastic properties, which may contribute to the variation in hysteresis. A quadratic curve fit was applied to the forward loading and reverse loading curves to calculate the hysteresis levels. Only the forward loading curves were shown with the data points in all the plots in Figure 6. The hysteresis levels were lower for smaller maximum deformation of the soft actuators.

Soft sensor. For static characterization of the soft sensor, the setup in Figure 4b-right was utilized. The linear actuator was run at a constant speed producing ramp profiles for input pressure (curve in red), as shown in Figure 7a. The curve in green is the force output of the soft actuator as measured by the commercial force sensor. This force output was then sensed by

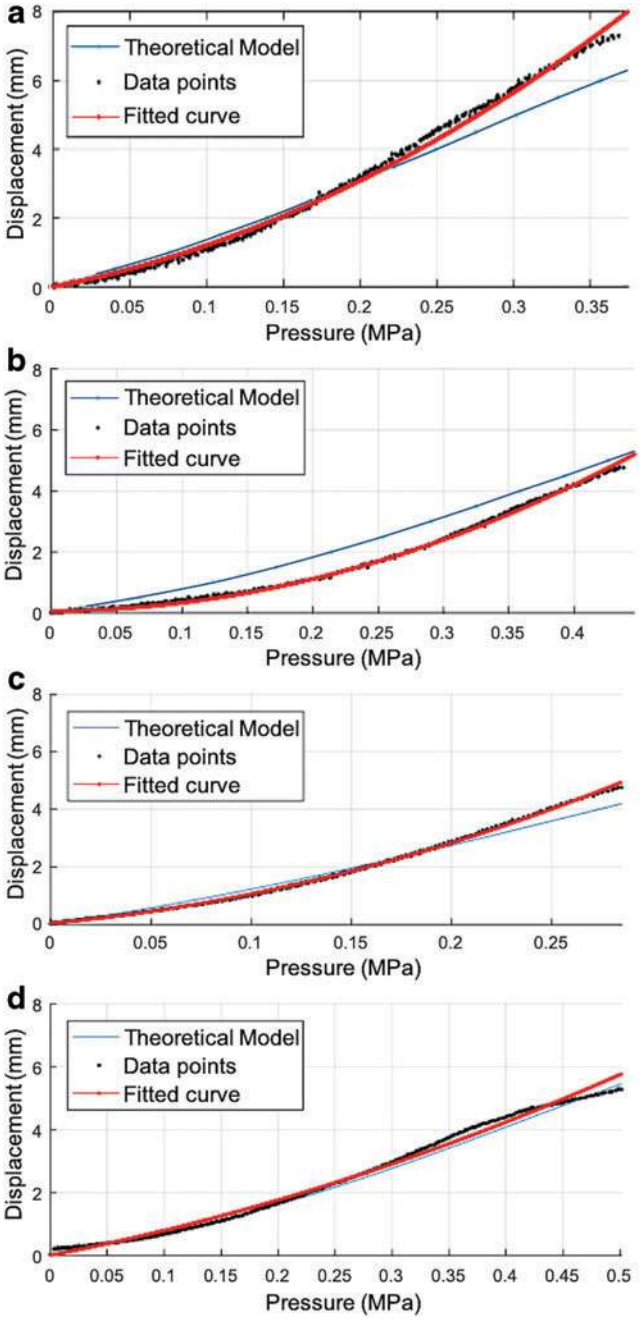

FIG. 6. Static calibration curve for soft actuators with E_a (100% tensile modulus reported in material data sheet) and E_a^{expr} (experimental modulus obtained from experimental data): **(a)** $E_a = 0.614$ MPa; $E_a^{expr} = E_a \cdot 1.8$ and $B = 1.3$ mm. **(b)** $E_a = 0.614$ MPa; $E_a^{expr} = E_a \cdot 1.8$ and $B = 1.8$ mm. **(c)** $E_a = E_a^{expr} = 1.173$ MPa and $B = 1.3$ mm. **(d)** $E_a = E_a^{expr} = 1.173$ MPa and $B = 1.8$ mm. Color images are available online.

the soft sensor, and the corresponding output is shown in Figure 7a (curve in blue). The same trial was repeated 10 times to collect extended datasets. The soft miniaturized actuation and sensing unit can produce and detect a force output within the range of 0–0.4 N, as shown in Figure 7a. Higher force output and sensing above 0.4 N are possible if the applied pressure is higher than in Figure 7a and the soft actuator is constrained, for example, within a catheter sheath.

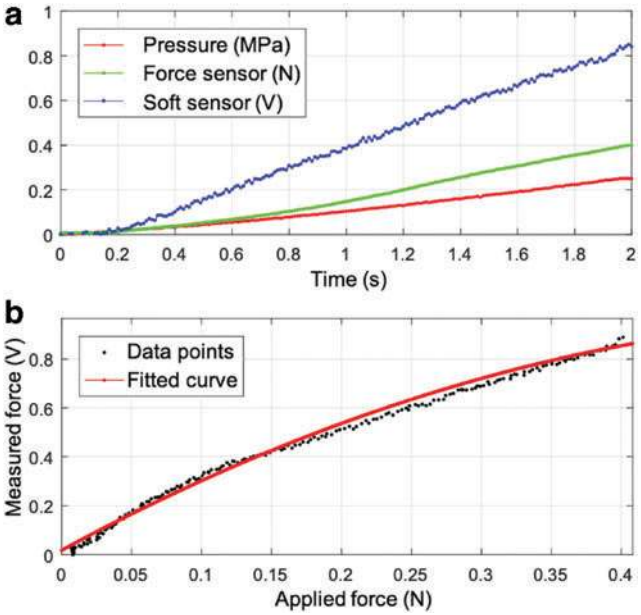

FIG. 7. **(a)** Pressure input (*red*), corresponding actuator force output (*green*), and force as measured by soft sensor (*blue*). **(b)** Soft sensor static calibration curve. Color images are available online.

Figure 7b shows the result of the calibration experiment. The data points in black show the force sensed by the soft sensor in volts and are representative data among the 10 data sets. A quadratic curve was fitted to the experimental data from all the 10 trials taken together; the red curve shows the final fitted curve. The RMSE and the coefficient of determination (R-squared) for the fit are 0.031 V and 0.987, respectively. The hysteresis error for the soft sensor was 10.6%. A quadratic curve fit was applied to the forward loading and reverse loading curves to calculate the hysteresis. Only the forward loading curves are shown with the data points in Figure 7b.

For determination of the resolution of the sensor, the data in Figure 7b were divided into samples of ~ 0 to 0.01 N and with the initial value deducted. This input data set had a mean value of 0.012 N with a standard deviation of 9.7×10^{-4} N. The corresponding output from the soft sensor had a mean value of 0.026 V with a standard deviation of 0.012 V.

Dynamic characterization

This section describes the experimental results validating the dynamic bandwidth requirements for the soft actuator and sensor. A series of sinusoidal displacement signals ranging from [0.2, 0.5, 1, 1.1, 1.2, 1.3, 1.4, 1.5] Hz with peak-to-peak amplitudes of 2 mm were applied. The pressures required to produce these displacements, based on the theoretical model, were passed as inputs to the controller. The signals were applied from a baseline of 0.2 Hz and going up to 1.5 Hz to determine if there was an appreciable decrease in the system response, both for the soft sensor and soft actuator.

Soft actuator. For the soft actuator, it is important to have a system bandwidth in the range of 1–2 Hz for a displacement in the range of 1–2 mm (corresponding to heart wall movement dynamics). The soft actuator with $E_a = 0.614$ MPa and $B = 1.3$ mm was subjected to sinusoidal excitations to determine its bandwidth. Figure 8a and b shows the response to the baseline 0.2 Hz and maximum 1.5 Hz sinusoidal excitation. The displacement vs. pressure plot for this result is shown in Figure 8c for evaluation of the level of hysteresis for both frequencies.

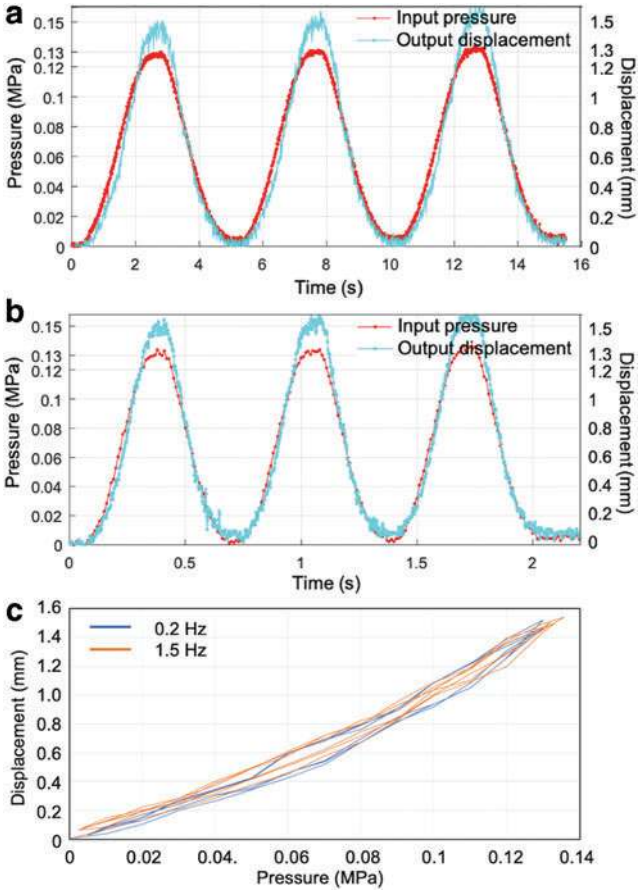

FIG. 8. Soft actuator response to sinusoidal input for dynamic characterization **(a)** at 0.2 Hz and **(b)** at 1.5 Hz. **(c)** Loading-unloading loops for frequencies 0.2 and 1.5 Hz. Color images are available online.

The curve in red shows the pressure input of ~ 0.13 MPa peak value, which is same for both 0.2 and 1.5 Hz. The resulting system response is ~ 1.5 mm peak value for both 0.2 and 1.5 Hz indicating that the system response does not decrease at higher frequencies and has at least a bandwidth of 1.5 Hz.

Soft sensor. The soft sensor should have a bandwidth in range of 1–2 Hz for a force range between 0.2 and 0.3 N observed during cardiac ablation procedures. Figure 9a and b shows the response to the baseline 0.2 Hz and maximum 1.5 Hz sinusoidal excitation. The curve in green shows the generated force output of ~ 0.25 N peak value, which is the same for both 0.2 and 1.5 Hz excitation. The curve in cyan color shows the raw force data from the soft sensor in volts, whereas the curve in blue shows the force data from the soft sensor in newtons after calibration. The resulting system response was ~ 0.52 V peak value for both 0.2 and 1.5 Hz

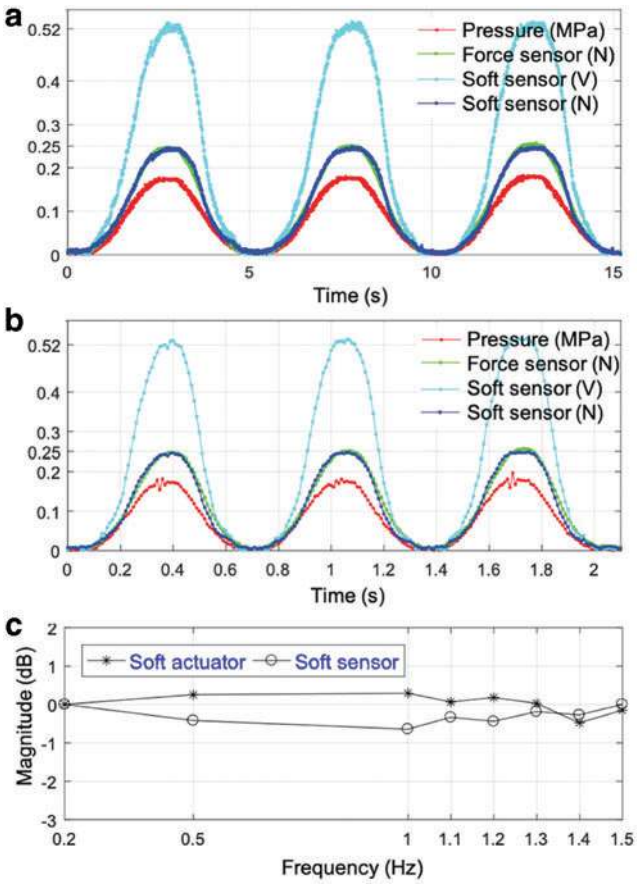

FIG. 9. Soft sensor response to sinusoidal input for dynamic characterization **(a)** at 0.2 Hz and **(b)** at 1.5 Hz. **(c)** Bode magnitude versus frequency plot for soft actuator and sensor for frequency range [0.2, 0.5, 1, 1.1, 1.2, 1.3, 1.4, 1.5]. Color images are available online.

indicating that the system response did not decrease at higher frequencies and has at least a bandwidth of 1.5 Hz.

Figure 9c shows the variations of the soft actuator and sensor responses at different frequencies up to 1.5 Hz. The phase of the output was approximately zero for all frequencies within the range 0.2–1.5 Hz, as can also be seen from Figures 8 and 9.

Preliminary force control results

The objective of this subsection is to describe how a simple proportional feedback controller could be used to ensure safety in AF procedures. In other words, the contact force levels are maintained within a certain safe range even during tissue motion. A soft silicone piece (Dragon Skin 30; Smooth-On, Inc.) was used to simulate the heart tissue compliance and was placed between the commercial force sensor and the catheter tip. The commercial force sensor was used to measure the ground truth values of the contact force and to compare it with the catheter tip sensor values. A heart tissue phantom was attached to a linear stepper motor. The stepper motor and phantom were used to simulate the sinusoidal trajectory of the heart wall due to the heartbeat. Figure 10 top describes the components of the force control setup.

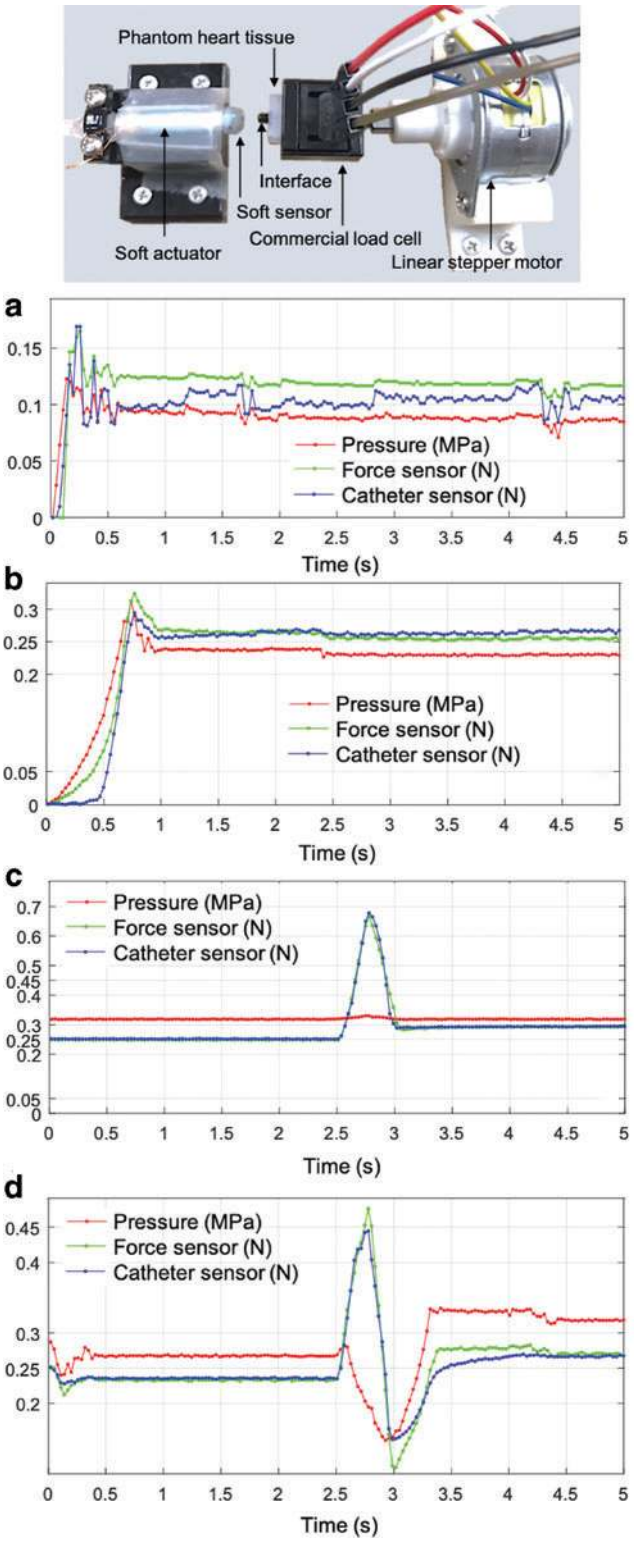

FIG. 10. Force control setup (*top*) and results. Tracking force control results without phantom tissue movement **(a)** for 0.1 N and **(b)** for 0.25 N. Force control results with tissue movement, which was not fed into the controller, with force controller **(c)** off and **(d)** on. Color images are available online.

Figure 10a and b depicts the control results of set-point force tracking without phantom tissue movement. In this test, initially the soft actuator made no contact with the phantom tissue. It gradually approached the tissue to make a contact and then tried to keep the contact force levels at 0.1 N (Fig. 10a) and 0.25 N (Fig. 10b). Forces were tracked close to the desired values, and the catheter force sensor values (blue line) also closely correlated with the ground truth values measured by the commercial force sensor (green line).

Figure 10c and d shows the force control results with the tissue movement, but the tissue movement actuated by the stepper motor was not fed into the controller. The stepper motor was used only for simulating the heart movement, and its input was not provided for the controller. The controller only reacted to the force measured by the eGaIn tip force sensor. For this experiment, the soft actuator was already making a contact with the tissue, and the interface was prestressed at 0.25 N. With a baseline contact force of 0.25 N the heart phantom moved with a speed of 4 mm/s with a displacement of 1.5 mm close to 2.5 s against the soft catheter unit and then back to its original position.

When the force controller was off (Fig. 10c), the phantom tissue movement led to excessive contact force close to 0.7 N. With the force controller on (Fig. 10d), the contact force was brought down to a much lower level, $\sim$0.45 N, and later contact force was tracked close to 0.25 N beyond 3 s, when no tissue movement was applied.

Discussion and Conclusion

In this work, we designed a series of soft miniaturized actuation and sensing units varying in size and material, which met the challenging requirement specifications for the cardiac ablation procedures with respect to compactness and integration. The embedded microfluidic sensor system was fabricated using eGaIn. Although eGaIn has low toxicity, future designs will focus on identifying optimal nontoxic biocompatible alternatives, such as sensing based on optical fiber[19,45] or sensing based on ionic liquid.[46–48] During contact force control, proper contact between the heart wall and the catheter tip was assumed, allowing for a one-DOF force measurement system.

In this proposed design, the catheter control from outside still lies with the cardiac physiologist. The advantage of this lies in the fact that the physician can adjust the orientation of the catheter tip using an adjustable sheath to minimize off-axis errors in placement, before fixing the system in place. However, the overall system design and workflow can be improved through the introduction of multimodal sensing (i.e., displacement and three-axis force). In addition, an anchoring mechanism can help secure the tip close to the heart wall.

An experimental setup, using hydraulic actuation for safety as opposed to pneumatic actuation typical of PAMs, was developed and used to characterize and control the prototyped units. However, a few issues must be addressed before the proposed system can be used in clinical settings.

The inlet tubing must have a smaller diameter to allow for the passage of electrode and sensing wires. Depending upon the length and the inner diameter of the tubing used for the hydraulic transmission, frictional losses might not be negligible. These losses would need to be calculated and the corresponding pressure loss would then need to be estimated for more accurate force control at the soft catheter tip.

Before clinical use, future work required includes the design of a modified catheter and the corresponding integration of the soft catheter tips. The modified catheter design would need to keep the same form and factor as traditional catheters, so as to be compatible with the current AF techniques. The inclusion of the wiring for the RF ablation electrodes and the microchannels for dispersing the X-ray contrast agent also would need to be considered. One possible modified catheter design could be along the lines of multisegment cardiac catheter steering mechanism presented in this work.[49]

Through experimental characterization, we have demonstrated that the soft miniaturized units met the static and dynamic performance requirements for the cardiac ablation procedures. Moreover, a theoretical model of soft thick-walled cylindrical actuators was developed, which could be used for prediction of static and dynamic performance for a parametric design evaluation.

We used an inexpensive linear stepper motor (LP25–35; Nanotec) which drives the syringe and is responsible for generating the hydraulic pressure driving the soft catheter actuator against the external load. It would be recommended to use a high-quality linear direct current (DC) motor with a much higher bandwidth, especially for force control experiments.

The effect of the low bandwidth of the stepper motor was clearly visible in the preliminary force control experimental results. While the contact force tracking worked well, as shown in Figure 9a and b, when the level of external force was low (0.1 – 0.25 N), the linear stepper motor was not fast enough to keep up at higher load levels of 0.4 – 0.7 N. Therefore, even with the force controller on, the level of interaction forces decreased enough (from $\sim$0.7 to 0.45 N) but not close to 0.25 N, as shown in Figure 9c and d. The contact force kept decreasing to the effect of almost no contact before recovering contact around 3 s; this observation also supports the finding that the linear stepper motor should be replaced by a DC motor with much higher bandwidth for better force control results.

Even though these actuation and sensing units were developed for targeted requirements of cardiac ablation procedures, a parametric design approach with different materials and sizes was presented, which could be tailored for other applications as well with requirement specification having similar orders of magnitude. The future work consists of developing force control strategies with these miniaturized units and demonstration of the same under various user case scenarios and cadaver studies using a modified overall catheter design. Another area of future work includes the development of multiaxis force sensing units in the limited space of the catheter tip, which will enable detection of the orientation of the tip to the wall.

Acknowledgment

The authors thank Mr. Luis Valle for his technical support in this research.

Author Disclosure Statement

No competing financial interests exist.

Funding Information

This work was supported, in part, by the National Heart, Lung, and Blood Institute (NHLBI), National Institutes of Health (NIH), United States, under Grant R21HL126081, and, in part, by the National Research Foundation (NRF) Grant funded by the Korean Government (MSIT), under Grant NRF-2016R1A5A1938472.

References

1. Strickland E. Medical robots go soft. IEEE Spectrum 2017; 54:11–12.
2. Kwon J, Park JH, Ku S, *et al.* A soft wearable robotic orthosis for ankle rehabilitation of post-stroke patients. IEEE Robot Autom Lett 2019;4:2547–2552.
3. Ansari Y, Manti M, Falotico E, *et al.* Towards the development of a soft manipulator as an assistive robot for personal care of elderly people. Int J Adv Robot Syst 2017;14: 1729881416687132.
4. Koh TH, Cheng N, Yap HK, *et al.* Design of a soft robotic elbow sleeve with passive and intent-controlled actuation. Front Neurosci 2017;11:597.
5. Oguntosin VW, Mori Y, Kim H, *et al.* Design and validation of exoskeleton actuated by soft modules toward neurorehabilitation–vision-based control for precise reaching motion of upper limb. Front Neurosci 2017;11:352.
6. Russo S, Ranzani T, Gafford J, *et al.* Soft pop-up mechanisms for micro surgical tools: Design and characterization of compliant millimeter-scale articulated structures. In: Proceedings of the IEEE International Conference on Robotics and Automation (ICRA), Stockholm, Sweden, May 2016, pp. 750–757.
7. Ranzani T, Cianchetti M, Gerboni G, *et al.* A soft modular manipulator for minimally invasive surgery: design and characterization of a single module. IEEE Trans Robot 2016;32:187–200.
8. Yim S, Goyal K, Sitti M. Magnetically actuated soft capsule with the multimodal drug release function. IEEE/ASME Trans Mechatron 2013;18:1413–1418.
9. Pazouki A. Minimally invasive surgical sciences: a new scientific opportunity for all scientists. J Minimally Invasive Surg Sci 2012;1:9–10.
10. Hu JC, Gu X, Lipsitz SR, *et al.* Comparative effectiveness of minimally invasive vs open radical prostatectomy. JAMA 2009;302:1557–1564.
11. Dooley A, Asimakopoulos G. Does a minimally invasive approach result in better pulmonary function postoperatively when compared with median sternotomy for coronary artery bypass graft? Interact Cardiovasc Thorac Surg 2013;16:880–885.
12. Stoianovici D, Kim C, Srimathveeravalli G, *et al.* MRI-safe robot for endorectal prostate biopsy. IEEE/ASME Trans Mechatron 2014;19:1289–1299.
13. Park YL, Elayaperumal S, Daniel B, *et al.* Real-time estimation of 3-D needle shape and deflection for MRI-guided interventions. IEEE/ASME Trans Mechatron 2010;15:906–915.
14. Yoshida K, Aonuma K. Catheter ablation of atrial fibrillation: past, present, and future directions. J Arrhythmia 2012; 28:83–90.
15. Haines DE. Determinants of lesion size during radiofrequency catheter ablation: the role of electrode-tissue contact pressure and duration of energy delivery. J Cardiovasc Electrophysiol 1991;2:509–515.
16. Shah DC, Leo G, Aeiby N, *et al.* Evaluation of a new catheter sensor for real-time measurement of tissue contact. Heart Rhythm 2006;3:S75–S76.
17. Yokoyama K, Nakagawa H, Shah DC, *et al.* Novel contact force sensor incorporated in irrigated radiofrequency ablation catheter predicts lesion size and incidence of steam pop and thrombus. Cir Arrhythmia Electrophysiol 2008;1:354–362.
18. Cappato R, Calkins H, Chen SA, *et al.* Worldwide survey on the methods, efficacy, and safety of catheter ablation for human atrial fibrillation. Circ 2005;111:1100–1105.
19. Polygerinos P, Seneviratne LD, Razavi R, *et al.* Triaxial catheter-tip force sensor for MRI-guided cardiac procedures. IEEE/ASME Trans Mechatron 2013;18:386–396.
20. Puangmali P, Althoefer K, Seneviratne LD, *et al.* State-of-the-art in force and tactile sensing for minimally invasive surgery. IEEE Sens J 2008;8:371–381.
21. Kesner SB, Howe RD. Force control of flexible catheter robots for beating heart surgery. In: Proceedings of the IEEE International Conference on Robotics and Automation (ICRA), Shanghai, China, May 2011, pp. 1589–1594.
22. Gelman D, Skanes AC, Tavallaei MA, *et al.* Design and evaluation of a catheter contact-force controller for cardiac ablation therapy. IEEE Trans Biomed Eng 2016;63:2301–2307.
23. Aranda-Michel E, Yi J, Wirekoh J, *et al.* Miniaturized robotic end-effector with piezoelectric actuation and fiber optic sensing for minimally invasive cardiac procedures. IEEE Sens J 2018;18:4961–4968.
24. Park YL, Majidi C, Kramer R, *et al.* Hyperelastic pressure sensing with a liquid-embedded elastomer. J Micromech Microeng 2010;20:125029.
25. Park YL, Chen BR, Wood RJ. Design and fabrication of soft artificial skin using embedded microchannels and liquid conductors. IEEE Sens J 2012;12:2711–2718.
26. Mengüç Y, Park YL, Pei H, *et al.* Wearable soft sensing suit for human gait measurement. Int J Robot Res 2014;33: 1748–1764.
27. Kim JH, Kim S, So JH, *et al.* Cytotoxicity of gallium–indium liquid metal in an aqueous environment. ACS Appl Mater Interfaces 2018;10:17448–17454.
28. Wang Q, Yu Y, Yang J, *et al.* Fast fabrication of flexible functional circuits based on liquid metal dual-trans printing. Adv Mater 2015;27:7109–7116.
29. Jin C, Zhang J, Li X, *et al.* Injectable 3-D fabrication of medical electronics at the target biological tissues. Sci Rep 2013;3:3442.
30. Guo C, Yu Y, Liu J. Rapidly patterning conductive components on skin substrates as physiological testing devices via liquid metal spraying and pre-designed mask. J Mater Chem B 2014;2:5739–5745.
31. Wirekoh J, Valle L, Pol N, *et al.* Sensorized flat pneumatic artificial muscles (sFPAM) embedded with biomimetic microfluidic sensors for proprioceptive feedback. Soft Robot 2019;6:768–777.
32. Niiyama R, Sun X, Sung C, *et al.* Pouch motors: printable soft actuators integrated with computational design. Soft Robot 2015;2:59–70.
33. Edler I, Hertz CH. The use of ultrasonic reflectoscope for the continuous recording of the movements of heart walls. 1954. Clin Physiol Funct Imaging 2004;24:118–136.
34. Dirschinger J, Kastrati A, Neumann FJ, *et al.* Influence of balloon pressure during stent placement in native coronary arteries on early and late angiographic and clinical outcome: a randomized evaluation of high-pressure inflation. Circulation 1999;100:918–923.

35. Felt W, Chin KY, Remy CD. Contraction sensing with smart braid McKibben muscles. IEEE/ASME Trans Mechatron 2016;21:1201–1209.
36. Robinson RM, Kothera CS, Sanner RM, *et al.* Nonlinear control of robotic manipulators driven by pneumatic artificial muscles. IEEE/ASME Trans Mechatron 2016;21:55–68.
37. Robinson RM, Kothera CS, Wereley NM. Variable recruitment testing of pneumatic artificial muscles for robotic manipulators. IEEE/ASME Trans Mechatron 2015;20: 1642–1652.
38. Li H, Kawashima K, Tadano K, *et al.* Achieving haptic perception in forceps' manipulator using pneumatic artificial muscle. IEEE/ASME Trans Mechatron 2013;18: 74–85.
39. Haughton DM, Ogden RW. Bifurcation of inflated circular cylinders of elastic material under axial loading—I. Membrane theory for thin-walled tubes. J Mech Phys Solids 1979;27:179–212.
40. Tondu B. Modelling of the McKibben artificial muscle: a review. J Intell Mater Syst Struct 2012;23:225–253.
41. Polygerinos P, Wang Z, Overvelde JTB, *et al.* Modeling of soft fiber-reinforced bending actuators. IEEE Trans Robot 2015;31:778–789.
42. Bishop-Moser J, Kota S. Design and modeling of generalized fiber-reinforced pneumatic soft actuators. IEEE Trans Robot 2015;31:536–545.
43. Haughton DM, Ogden RW. Bifurcation of inflated circular cylinders of elastic material under axial loading—II. Exact theory for thick-walled tubes. J Mech Phys Solids 1979;27: 489–512.
44. Zhu Y, Luo XY, Ogden RW. Asymmetric bifurcations of thick-walled circular cylindrical elastic tubes under axial loading and external pressure. Int J Solids Struct 2008;45: 3410–3429.
45. Noh Y, Liu H, Sareh S, *et al.* Image-based optical miniaturized three-axis force sensor for cardiac catheterization. IEEE Sens J 2016;16:7924–7932.
46. Russo S, Ranzani T, Liu H, *et al.* Soft and stretchable sensor using biocompatible electrodes and liquid for medical applications. Soft Robot 2015;2:146–154.
47. Choi DY, Kim MH, Oh YS, *et al.* Highly stretchable, hysteresis-free ionic liquid-based strain sensor for precise human motion monitoring. ACS Appl Mater Interfaces 2017; 9:1770–1780.
48. Chossat JB, Shin HS, Park YL, *et al.* Soft tactile skin using an embedded ionic liquid and tomographic imaging. ASME J Mech Robot 2015;7:021008.
49. Ataollahi A, Karim R, Fallah AS, *et al.* Three-degree-of-freedom MR-compatible multisegment cardiac catheter steering mechanism. IEEE Trans Biomed Eng 2016;63: 2425–2435.

Address correspondence to:
Yong-Lae Park
Department of Mechanical Engineering
Institute of Advanced Machines and Design
Institute of Engineering Research
Seoul National University
Seoul 08826
Korea

E-mail: ylpark@snu.ac.kr